

Superconductivity of underdoped PrFeAs(O,F) investigated via point-contact spectroscopy and nuclear magnetic resonance

*Original*

Superconductivity of underdoped PrFeAs(O,F) investigated via point-contact spectroscopy and nuclear magnetic resonance / Daghero, Dario; Piatti, Erik; Zhigadlo, Nikolai D.; Ummarino, Giovanni A.; Barbero, Nicolò; Shiroka, Toni. - In: PHYSICAL REVIEW. B. - ISSN 2469-9969. - STAMPA. - 102:(2020), p. 104513. [10.1103/PhysRevB.102.104513]

*Availability:*

This version is available at: 11583/2847020 since: 2020-09-29T14:56:09Z

*Publisher:*

American Physical Society

*Published*

DOI:10.1103/PhysRevB.102.104513

*Terms of use:*

This article is made available under terms and conditions as specified in the corresponding bibliographic description in the repository

*Publisher copyright*

(Article begins on next page)

# Superconductivity of underdoped PrFeAs(O,F) investigated via point-contact spectroscopy and nuclear magnetic resonance

D. Daghero<sup>\*</sup> and E. Piatti<sup>†</sup>

*Department of Applied Science and Technology, Politecnico di Torino, 10129 Torino, Italy*

N. D. Zhigadlo<sup>‡</sup>

*CrystMat Company, CH-8046 Zurich, Switzerland*

G. A. Ummarino<sup>§</sup>

*Department of Applied Science and Technology, Politecnico di Torino, 10129 Torino, Italy*

*and National Research Nuclear University MEPhI (Moscow Engineering Physics Institute), Kashira Highway 31, Moskva 115409, Russia*

N. Barbero and T. Shiroka<sup>§</sup>

*Laboratory for Muon-Spin Spectroscopy, Paul Scherrer Institut, CH-5232 Villigen PSI, Switzerland*

*and Laboratorium für Festkörperphysik, ETH Zürich, CH-8093 Zurich, Switzerland*



(Received 9 June 2020; revised 28 August 2020; accepted 8 September 2020; published 28 September 2020)

Underdoped PrFeAs(O,F), one of the lesser known members of the 1111 family of iron-based superconductors, was investigated in detail by means of transport, magnetometry, nuclear magnetic resonance (NMR) measurements, and point-contact Andreev-reflection spectroscopy (PCARS). PCARS measurements on single crystals evidence the multigap nature of PrFeAs(O,F) superconductivity, shown to host at least two isotropic gaps, clearly discernible in the spectra, irrespective of the direction of current injection (i.e., along the *ab* planes or along the *c* axis). Additional features at higher energy can be interpreted as signatures of a strong electron-boson coupling, as demonstrated by a model which combines Andreev reflection with the Eliashberg theory. Magnetic resonance measurements in the normal phase indicate the lack of a magnetic order in underdoped PrFeAs(O,F), while <sup>75</sup>As NMR spin-lattice relaxation results suggest the presence of significant electronic spin fluctuations, peaking above *T<sub>c</sub>* and expected to mediate the superconducting pairing.

DOI: [10.1103/PhysRevB.102.104513](https://doi.org/10.1103/PhysRevB.102.104513)

## I. INTRODUCTION

The discovery of superconductivity in *Ln*FeAsO oxypnictides (*Ln*1111, *Ln*: lanthanide) generated a widespread interest among the condensed matter physicists [1]. These compounds, which belong to the 1111 family of Fe-based superconductors, exhibit a ZrCuSiAs-type structure, composed of alternating stacks of *Ln*O and FeAs layers. They become superconductors either through chemical substitution at different atomic sites, or through the application of external pressure [2–4]. Consequently, the resulting electronic phase diagrams depend sensitively on the particular doping element. In either case, the original antiferromagnetic state is partially or fully suppressed. In particular, it has been shown that the *Ln*FeAsO parent compounds can be doped with holes by partially replacing the *Ln*<sup>3+</sup> ions with divalent ions, such as Sr<sup>2+</sup>, as, e.g., in La<sub>1–*x*</sub>Sr<sub>*x*</sub>FeAsO [5] or Pr<sub>1–*x*</sub>Sr<sub>*x*</sub>FeAsO [6]. In contrast, *n*-type doping can be achieved by substituting *Ln*<sup>3+</sup> with tetravalent ions, such as Th<sup>4+</sup> (Sm<sub>1–*x*</sub>Th<sub>*x*</sub>FeAsO) [7,8], or by partially replacing O<sup>2–</sup> with F<sup>–</sup> or H<sup>–</sup> (*Ln*FeAsO<sub>1–*x*</sub>F<sub>*x*</sub>,

*Ln*FeAsO<sub>1–*x*</sub>H<sub>*x*</sub>) [2,3]. In addition, in the case of isovalent doping of the *Ln*1111 parent compound, as, e.g., in the As<sub>1–*x*</sub>P<sub>*x*</sub> case, one can tune the magnetic interactions without changing the carrier concentration [9,10]. Until now, the electron-doped *Ln*1111-type oxypnictides (O<sub>1–*x*</sub>F<sub>*x*</sub> and O<sub>1–*x*</sub>H<sub>*x*</sub>) seem to exhibit the highest *T<sub>c</sub>*'s. The control of *T<sub>c</sub>* through carrier concentration is, therefore, a versatile and powerful mean of elucidating the intrinsic nature of superconductivity.

In most *Ln*1111 families, an increase in doping level shifts the system from an antiferromagnetically (AF) ordered state towards a purely superconducting (SC) state via a region where the AF and SC phases coexist [11–13]. By contrast, in PrFeAsO<sub>1–*x*</sub>F<sub>*x*</sub>, the Néel order (and the tetragonal-to-orthorhombic structural transition) appear to vanish rather rapidly, possibly in a first-order-type transition, as the fluorine concentration approaches the critical value *x* ~ 0.08 [14]. This behavior has been observed to occur also in the LaFeAsO<sub>1–*x*</sub>F<sub>*x*</sub> family [15]. On the other hand, it differs significantly from the structurally related families (where the *Ln* ion is, e.g., Sm, Nd, Ce, etc.), whose AF-to-SC transitions are much more extended. To investigate this in further detail, homogeneously underdoped samples, preferentially in a single-crystalline form, are required.

<sup>\*</sup>dario.daghero@polito.it

<sup>†</sup>nzhigadlo@gmail.com

<sup>‡</sup>tshiroka@phys.ethz.ch

To date, despite extensive evidence that superconductivity in Fe-based materials is mediated by spin fluctuations, a conclusive experimental confirmation is still missing. In particular, the interplay between the AF fluctuations and superconductivity in the underdoped regime remains unclear, mainly reflecting the difficulties associated with the preparation of high-quality underdoped  $Ln1111$  samples. The first step toward the elucidation of the nature of superconductivity is the growth of high-quality crystals.

Here, we report on advanced point-contact Andreev reflection spectroscopy (PCARS) and nuclear magnetic resonance (NMR) studies of superconductivity in underdoped  $\text{PrFeAsO}_{1-x}\text{F}_x$  crystals with a  $T_c$  of  $\sim 24$  K. Through an exhaustive set of measurements, we directly assess the multigap nature of superconductivity in this compound and determine the amplitudes of the gaps that appear to be isotropic in-plane and out-of plane, with no evidence of extended node lines. We bring evidence of a strong coupling between electrons and a bosonic mode whose characteristic energy agrees well with that of spin fluctuations. Finally, we show that the magnetic order, typical of the parent compounds, is completely suppressed in these underdoped crystals, while sizable spin fluctuations persist, as indicated by NMR. Altogether, these results strongly point towards a spin-fluctuation-mediated multiband superconductivity in  $\text{PrFeAsO}_{1-x}\text{F}_x$ .

## II. CRYSTAL GROWTH AND EXPERIMENTAL DETAILS

The  $\text{PrFeAs}(\text{O},\text{F})$  crystals were grown by using a cubic-anvil high-pressure high-temperature technique. The details of the setup can be found in Refs. [16,17]. Starting powders of  $\text{PrAs}$ ,  $\text{FeF}_2$ ,  $\text{Fe}_2\text{O}_3$ , and  $\text{Fe}$  of high purity ( $\geq 99.95\%$ ) were weighed according to the stoichiometric ratio, thoroughly grounded in a mortar and then mixed with  $\text{NaAs}$  flux. For one growth batch we used 0.45 g of  $\text{PrFeAsO}_{0.60}\text{F}_{0.35}$  and 0.2 g of  $\text{NaAs}$ . The crystal growth process was performed by heating the mixture up to  $\sim 1500^\circ\text{C}$  in 2 h. The mixture was kept there for 5 h, cooled to  $1250^\circ\text{C}$  in 60 h, held at this temperature for 3 h, and finally cooled down to room temperature. The crystalline products were separated by dissolving the flux in distilled water. Further details on the crystal growth of  $\text{PrFeAs}(\text{O},\text{F})$  can be found in Ref. [17].

The x-ray analysis confirmed that the obtained crystals belong to the 1111-type structure, with the refined model being consistent with that from our previous x-ray diffraction studies (see Table I in Ref. [18]). Compositional analysis via energy-dispersive x-ray (EDX) measurements confirmed that the ratio of praseodymium, iron, and arsenic is close to 1:1:1. Light elements such as oxygen and fluorine cannot be measured accurately via EDX. Therefore, we could not determine the exact doping level of the  $\text{PrFeAs}(\text{O},\text{F})$  crystals. Nevertheless, by a comparison of our transition temperatures with those of polycrystalline samples [14] (see below), we estimate an  $F$  doping of  $\sim 0.1$  in our case.

The details of the PCARS technique are given in Appendix A. As for the NMR study, this consisted in  $^{75}\text{As}$  lineshape- and spin-lattice relaxation measurements, performed at 7.057 T over a temperature range from 4 to 295 K. The NMR signals were detected by means of standard spin-echo sequences, consisting in  $\pi/2$  and  $\pi$  pulses of 3 and 6  $\mu\text{s}$ ,

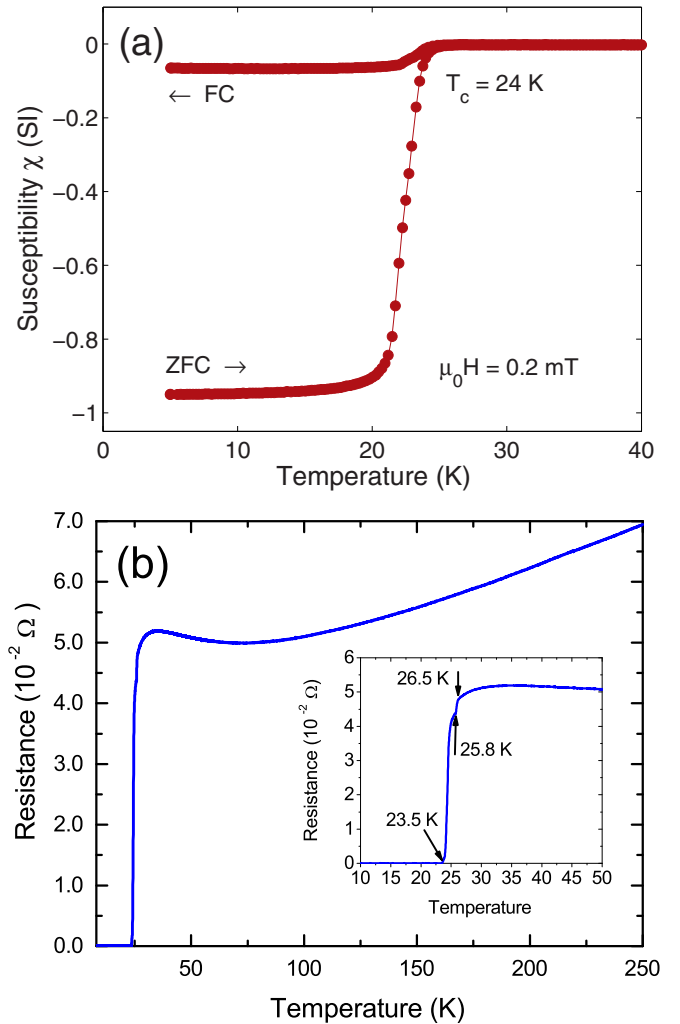


FIG. 1. (a) Temperature dependence of magnetic susceptibility of a single  $\text{PrFeAs}(\text{O},\text{F})$  crystal. The zero-field-cooled (ZFC) curve was obtained on heating in a magnetic field of 0.2 mT applied along the  $c$  direction. (b) Resistance as a function of temperature. The inset shows a closeup of the superconducting transition.

with recycling delays ranging from 0.01 to 1 s. The lineshapes were obtained via fast Fourier transform (FFT) of the echo signal. Spin-lattice relaxation times  $T_1$  were measured via inversion recovery, by using a  $\pi-\pi/2-\pi$  pulse sequence.

## III. SUPERCONDUCTING PROPERTIES

### A. Preliminary characterization of superconductivity

The dependence of magnetic susceptibility versus temperature in a single  $\text{PrFeAsO}_{1-x}\text{F}_x$  crystal, measured in a magnetic field of 0.2 mT parallel to the  $c$  axis, is shown in Fig. 1(a). Here, the effective superconducting transition temperature  $T_{c,\text{eff}}$  is defined as the crossing of the linear extrapolations from the two regions of the high-temperature normal state and low-temperature superconducting state. In the underdoped case the transition is relatively sharp, indicative of a good sample quality.

The resistance was measured by using a standard four-probe technique, with the current flowing in the  $ab$  plane.

Upon lowering the temperature, as shown in Fig. 1(b), the resistance first decreases linearly, to reach a broad minimum around 70 K, and then it increases again. Similar features were also observed in the other investigated crystals. A closeup of the superconducting transition region is shown in the inset. After a saturation around 30 K the resistance starts dropping and reaches its zero value at 23.5 K, fully consistent with the onset of the magnetic transition as measured via superconducting quantum interference device (SQUID) magnetometry. This behavior (and the relevant values) are similar to those observed in polycrystals with  $x = 0.11$  by Rotundu *et al.* [14]. A very tiny kink at 25.8 K might indicate the presence of another superconducting phase with a close-lying  $T_c$  value and, hence, with practically the same F doping. It is interesting to note that there seems to be a connection between the position of the minimum in the normal-state resistance and the critical temperature  $T_c$  (i.e., the two differ by a factor of about 3 in all the measured crystals).

### B. Superconducting energy gaps

Further insight into the superconducting properties of PrFeAs(O,F) is obtained from the point-contact Andreev reflection spectroscopy, which allows us to directly investigate the superconducting gap structure. The technique is quite simple and consists in measuring the differential conductance,  $dI/dV$ , of a point-like contact between a normal metal and the superconductor under study, as a function of the bias voltage  $V$  across the contact (see Appendix A for details).

Figure 2 shows typical conductance curves, measured at 2.7 K, for contacts made either on the top surface (*c*-axis contacts) or on the side (*ab* plane contacts). The labels refer to the direction of current injection, i.e., perpendicular or parallel to the FeAs planes, respectively. Despite the different shapes of the curves, the different directions of current injection, and the different resistance of the contacts, it is clear that they all show structures at approximately the same energies. In particular, the position of the low-energy maxima ( $\pm 3.5$  meV, solid vertical lines) is very robust. Additional features that can take the form of maxima, shoulders, or slope changes are present at about  $\pm 7.5$  mV (dashed vertical lines). These two values are particularly interesting because a full SC gap with an amplitude  $1.6k_B T_c = 3.5$  meV was observed in underdoped PrFeAs(O,F) single crystals by microwave penetration depth and by quasiparticle conductivity measurements [19], while a gap of  $3.5k_B T_c \simeq 7.5$  meV was detected by optical conductivity measurements [20]. Other structures whose occurrence is apparently less systematic can be observed at higher energies (arrows). From the spectroscopic point of view, the fact that there are structures whose position does not depend on the resistance of the contacts means that (i) all the contacts are spectroscopic, at least at low temperature and (ii) these structures are intrinsic, i.e., unrelated to the contact, but instead directly connected to the properties of the material. In particular, they are suggestive of the presence of multiple (at least two) superconducting energy gaps. This is a rather common feature of Fe-based systems (including here materials of the same family, such as La-1111 [21] and Sm-1111 [22]). It is worth noting also that the position of the spectral features does not depend on the direction of current injection, which

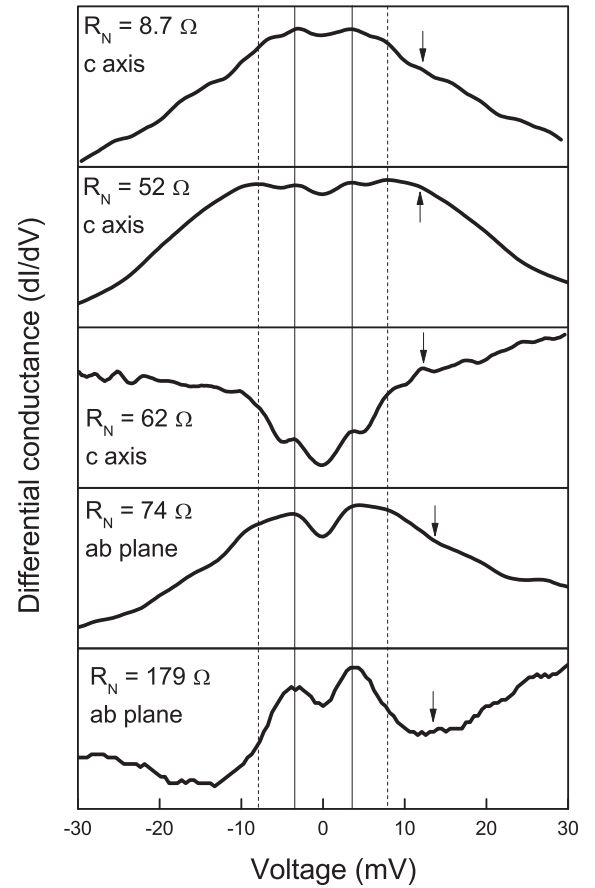


FIG. 2. Low-temperature (2.7 K) conductance curves for various contacts made on the same single crystal. Despite the different shapes, all the curves display structures (maxima, shoulders, slope changes) at approximately the same positions, as indicated by the vertical lines at  $\pm 3.5$  and  $\pm 7.5$  mV. Arrows indicate structures related to the strong electron-boson coupling.

suggests that the system does not show a clear in-plane/out-of-plane anisotropy, at least for the gap amplitudes. Clearly, one cannot exclude small anisotropies (i.e.,  $k$  dependence of the SC gaps), undetectable by our technique.

Finally, the shape of the curves and, in particular, the absence of zero-bias maxima indicates the absence of significant contributions of low-energy quasiparticles to the conductance, thus suggesting a fully gapped SC and the absence of node lines (as also demonstrated by microwave penetration depth measurements in underdoped single crystals [19]). A similar situation was observed in other 1111 compounds like F-doped Sm-1111 and La-1111 [21,22]. By contrast, the PCARS spectra of some 122 systems, featuring accidental node lines, show zero-bias maxima at least in one of the directions of current injection; a typical example being the Ca-122 system [23,24]. Based on the spectra shown in Fig. 2, and consistently with the results of penetration depth [19], critical field [19], infrared spectroscopy [20] and NMR [25] measurements, as well as with electronic band-structure calculations for 1111 compounds, from now on we will assume PrFeAs(O,F) to be a multiple-gap  $s\pm$ -wave superconductor.

Figure 3 shows the conductance curves of a 74-Ohm, *ab*-plane contact on a PrFeAs(O,F) single crystal as a function

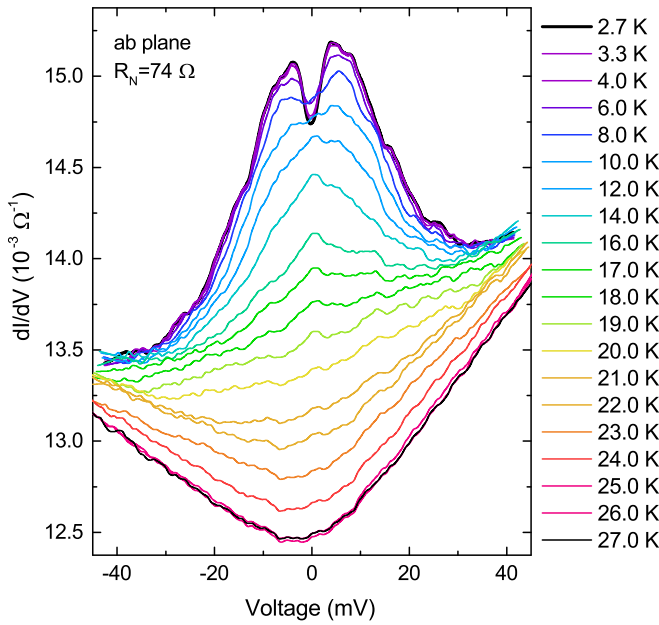


FIG. 3. Temperature dependence of the conductance curves of a 74- $\Omega$ , *ab*-plane contact on a PrFeAs(O,F) single crystal. Upon increasing  $T$ , the Andreev-reflection features decrease in amplitude and disappear between 24 and 25 K.

of temperature. The lowest-temperature spectrum was already depicted in the second-last panel of Fig. 2. The temperature dependence is crucial in identifying the critical temperature  $T_c^A$  where the Andreev signal disappears, thus allowing us to determine the normal-state conductance of the contact. As a matter of fact, the progressive decrease in amplitude of the spectra on increasing temperature is due to the decrease in amplitude of the superconducting gap(s). Hence,  $T_c^A$  can be identified with the temperature at which the curves recorded at increasing temperatures start to overlap and the Andreev-reflection features disappear. In our case, the gap vanishes between 24 and 25 K since the 25-K conductance curve is superimposed to those recorded at 26 and 27 K. Thus, the curve recorded at 25 K represents the normal-state spectrum of the contact and we will assume  $T_c^A = 24.5 \pm 0.5$  K. Note that this value is consistent with the  $T_c$  obtained from magnetometry and transport data (see Fig. 1). This, again, is an indirect, yet quite convincing proof of the spectroscopic nature of the contact. Indeed, if the conduction through the contact were diffusive, Joule heating would occur *within the contact* [26] and the Andreev signal would disappear at a lower bath temperature.

To extract the gap amplitudes more accurately, the conductance curves must first be normalized and then fitted to a suitable model. The normalization is obtained by dividing the differential conductance recorded at a given  $T < T_c$  by the normal-state conductance of the same contact. The curve measured just above  $T_c$  can be used, under the reasonable assumption that the normal-state properties do not change much between  $T$  and  $T_c$ . The lowest-temperature curve in Fig. 3, once divided by the normal-state curve recorded at 27 K (and symmetrized, to better highlight the intrinsic structures and to suppress noise fluctuations) is shown in Fig. 4(a) (circles). On

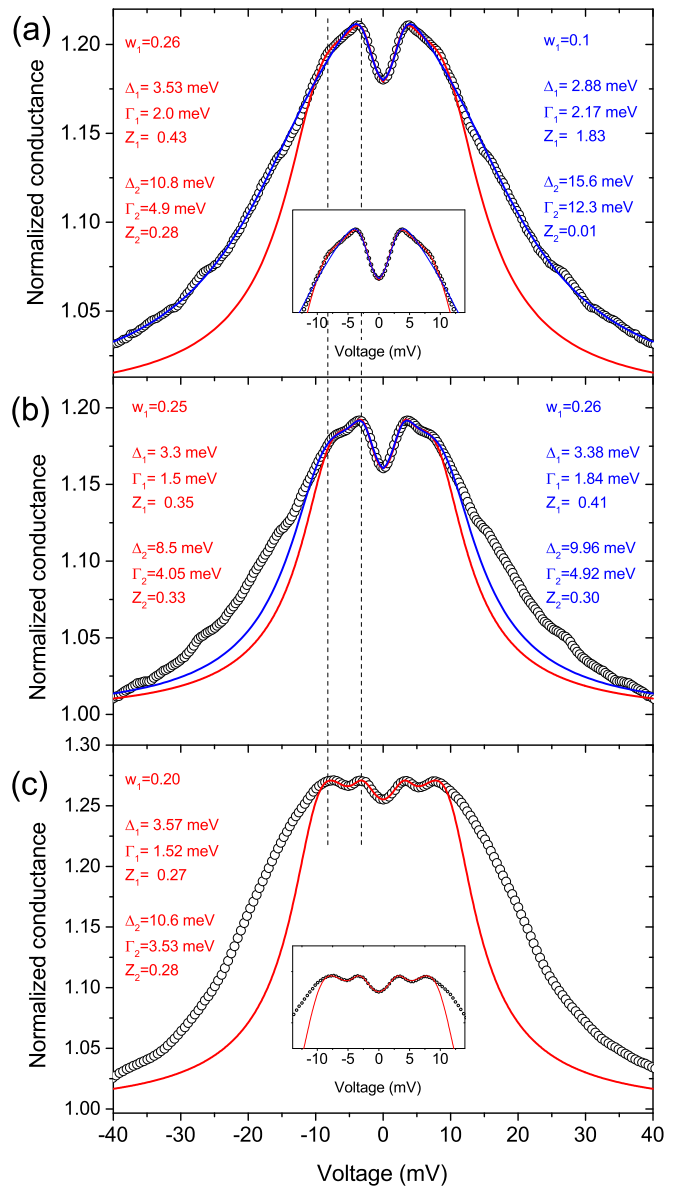


FIG. 4. (a) Open circles: low-temperature (2.7 K) conductance data of a 74- $\Omega$ , *ab*-plane contact on a PrFeAs(O,F) single crystal, after normalization (i.e., division by the normal-state conductance curve without any shift). The blue line is a two-gap fit of the whole curve. The red curve is a fit of the central part, excluding the wide shoulders associated to the electron-boson coupling structures. (b) Same curve as in (a), but with a different normalization (division by the normal-state conductance curve shifted upwards). The two fitting curves were obtained with different values of  $V_{\max}$ . (c) Normalized low-temperature conductance data of a *c*-axis, 52- $\Omega$  contact (circles) with the relevant best fit. Vertical dashed lines highlight the correspondence of the position of the gap structures.

top of it, we plot some theoretical curves, obtained through an automatic fitting procedure based on the minimization of the sum of squared residuals. The model used to fit the experimental data is a two-band, two-dimensional (2D) version of the Blonder-Tinkham-Klapwijk (BTK) model [26–28]. This model contains as free parameters the amplitude of the gaps  $\Delta_1$  and  $\Delta_2$ , the broadening parameters  $\Gamma_1$  and  $\Gamma_2$ , the barrier



parameters  $Z_1$  and  $Z_2$ , and the relative weight of band 1 in the conductance  $w_1$ . These parameters are not completely free because the values of the gaps reflect the position of the maxima and shoulders, and the barrier parameters determine the percentage of the tunnel versus Andreev-reflection conduction through the junction and, in practice, are related to the depth of the zero-bias minimum and to the shape of the curve between  $\Delta_1$  and  $\Delta_2$ . Details of the fitting procedure can be found elsewhere [26]. The blue curve in Fig. 4(a) is an attempt to fit the conductance data across the whole voltage range. The overall fit seems fairly good, yet the fitting function completely fails to reproduce the features at  $\pm 7.5$  mV, most likely reflecting a superconducting gap (see inset). Moreover, the amplitude of the large gap  $\Delta_2 = 15.6$  meV is far too big for a system with  $T_c = 25$  K since the gap ratio  $2\Delta_2/k_B T_c$  would be 14.5. This value is completely unreasonable even though, in other compounds of the 1111 family, the (larger) gap ratio can be as high as 8 [21,22]. Finally, the values of the  $\Gamma$  parameters are too high, and comparable to the gap values themselves, which should not happen in a spectroscopic contact. The fit is thus unsatisfactory and meaningless. The reason is that, as already demonstrated in the case of Ba(Fe, Co)<sub>2</sub>As<sub>2</sub> [29], SmFeAs(O,F) [30], and Fe(Te,Se) [31], in Fe-based superconductors the relatively strong coupling between the electrons and bosons that mediates the Cooper pairing gives rise to additional structures (shoulders) in the tunnel and PCARS spectra, better seen as peaks in the second derivative  $-d^2I/dV^2$ , that do *not* occur at the gap edge, but at a higher energy  $E_p$ . As discussed in Ref. [30], in the case of multiple gaps this energy is  $E_p \simeq \Delta_{\max} + \Omega_0$ , where  $\Omega_0$  is the characteristic boson energy and  $\Delta_{\max}$  is the largest gap. The electron-boson interaction does not affect the spectra in the energy region where the gap features are observed, but it gives rise to shoulders that can extend to rather high energies and can enormously enhance the apparent width of the conductance curve. These structures *cannot* be fitted by the Blonder-Tinkham-Klapwijk model, even in its various extended versions, if energy-independent gaps are used as in the BCS, weak-coupling theory. To include the effects of strong coupling in the theory, a much more complicated procedure has to be used, which involves the solution of the Eliashberg equations (see Appendix B). As demonstrated in Appendix B, since the BCS theory represents the low-energy limit of the Eliashberg theory, the low-bias region of the spectrum is completely and uniquely determined by the Andreev reflection. Hence, in this region, the BTK model with constant gaps can be safely used to extract the gap values [32]. In Fe-based compounds, the superconductivity is thought to be mediated by spin fluctuations. Indeed, the position of the electron-boson structures we observe in the aforementioned materials agrees well with a characteristic boson energy  $\Omega_0$  that obeys the empirical law  $\Omega_0 \simeq 2T_c/5$ , where  $T_c$  is in kelvin and  $\Omega_0$  in meV [33]. In our samples,  $\Omega_0 \simeq 10$  meV and the structures are expected to fall at energies larger than the maximum gap amplitude that we will call  $\Delta_2$ .

We have thus to abandon the idea of fitting the *whole* curve, and focus instead on the low-energy region that hosts the structures related to the gaps, i.e., on the region  $|V| \leq V_{\max}$ . The choice of  $V_{\max}$  is somewhat arbitrary and can (slightly) affect the values of the energy gaps. The red curve in Fig. 4(a)

was obtained by setting  $V_{\max} = 10$  mV, which implies much more reasonable values for the parameters (reported in the labels). In particular, the value of the small gap  $\Delta_1 = 3.53$  meV is perfectly compatible with the results of penetration depth and quasiparticle conductivity measurements [19].

The fact that the high-energy tails of the unnormalized curves (Fig. 3) are affected by the electron-boson structures, and the fact that these structures *depend* on the energy gap and disappear only at  $T_c$  [29,30], means that also the normalization is somewhat arbitrary. The usual criterion, i.e., that the high-voltage tails ( $V > 3\Delta_2$ ) of the conductance curves must fall on top of the normal-state conductance, is no longer true. To be conservative, we thus tried different normalizations, obtained by vertically shifting the normal-state conductance by different amounts. We found that the amplitude of the small gap is very robust, being determined by the energy position of the maxima, while the value of the large gap depends somewhat on the height of the normalized curve, that in turn depends on the normalization. For example, Fig. 4(b) reports the same curve, with a different normalization (i.e., divided by the normal-state conductance shifted slightly upwards) with two fits, obtained by using different values of  $V_{\max}$ . We will keep track of this variation by using proper error bars on the gap values.

Figure 4(c) shows the normalized low-temperature conductance curve of a 52- $\Omega$ , *c*-axis contact. As in the previous case, the curve presents maxima around 3 mV and structures at  $\sim 7.5$  meV that here appear as clear maxima. The fit, which disregards the shoulders clearly associated to the electron-boson structures, gives a small gap  $\Delta_1 = 3.57$  meV (in perfect agreement with what was found in the previous case) and a large gap  $\Delta_2 = 10.6$  meV, whose value exhibits a certain variability, depending on the normalization. In the spectrum shown in Fig. 5(a), recorded at 2.7 K in a *c*-axis contact with resistance 8.7  $\Omega$ , the features associated to the large gap are rather clear and well separated from the electron-boson structures. Here, the best fit gives  $\Delta_1 = 3.78$  meV and  $\Delta_2 = 7.63$  meV.

Figure 5(b) shows the low-temperature conductance curve of an *ab*-plane point contact on the same crystal. Here, the features related to the small gap are dominant and no clear structures associated to the large gap can be detected by eye. With the normalization shown in the figure (obtained without any shift of the normal-state conductance), the two-gap fit (red line) is superior to the single-gap one (blue line), because it can reproduce both the position of the maxima (see inset) and the width of the curve. This fit gives  $\Delta_1 = 3.68$  meV and  $\Delta_2 = 7.13$  meV. The gap value obtained by the single-band fit is  $\Delta = 5.03$  meV and can be seen as a sort of an average of  $\Delta_1$  and  $\Delta_2$ , as usually happens when multiple gaps are insufficiently resolved in the spectra. Actually, by choosing different normalizations, the single-band fit can become almost indistinguishable from the two-band one (in particular, if the amplitude of the normalized curve is lowered) and it always provides a gap  $\Delta$ , intermediate between  $\Delta_1$  and  $\Delta_2$ . Therefore, on the basis of this spectrum alone, one cannot decide between the single-band and the multiband picture. However, the two-gap picture is compatible with all the other spectra, and there is no reason to expect a different behavior in this particular case.

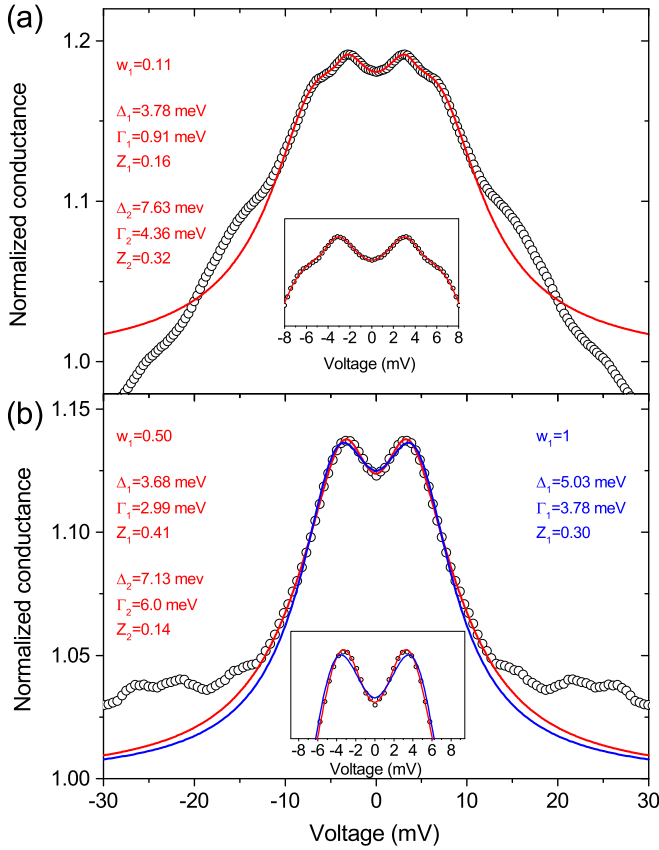


FIG. 5. (a) Normalized differential conductance at 2.7 K (circles) and relevant fit (red line) for a *c*-axis contact with a resistance of 8.7 Ω. (b) Open circles: low-temperature (2.7 K) conductance spectrum of a 179-Ω, *ab*-plane contact, divided by the normal-state conductance curve without any shift. The blue line is a single-gap fit, while the red curve is a two-gap fit, both made with  $|V_{\max}| = 10$  mV. The inset shows a closeup of the low-bias region.

Figures 4 and 5 are representative of all the datasets we collected: while the value of the small gap is always the same (within experimental uncertainties), the values of the large gap seem to fall into two energy intervals: one centered around 7 meV and another around 10 meV. In principle, this clustering could indicate that there are actually *two* different large gaps. The fact that we detect either one or the other may be due to the use of a *two*-gap fit function (a model with three gaps would have 12 free parameters, too many for the fit procedure to be meaningful). The presence of more than two gaps is not unusual for Fe-based superconductors, considering that in these compounds three or more bands cross the Fermi level.

Figure 6 summarizes the values of the gaps extracted from the fit of all the conductance datasets, as a function of the contact resistance. The value of the small gap is very well defined and completely independent of the resistance, which is the last and definitive proof that the contacts are spectroscopic. The values of the large gap(s) are more scattered and affected by the uncertainty arising from the aforementioned degree of freedom introduced by the electron-boson structures. These, although excluded from the fits, can still affect the normalization. The figure highlights also the energy range

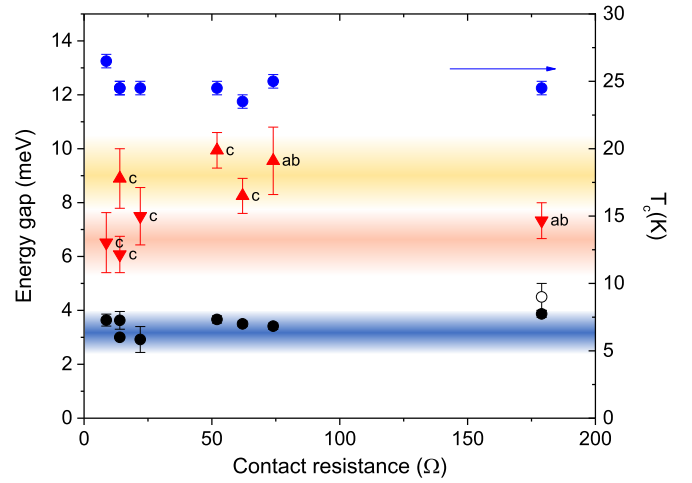


FIG. 6. Energy gaps (red and black solid symbols) and Andreev critical temperature (blue symbols) as a function of the contact resistance. The open symbol represents the result of a single-gap fit of the curve shown in Fig. 5(b). The labels indicate the type of contact (i.e., with current parallel to the *c* axis or to the *ab* planes).

where the SC gaps occur. As for the large gap, we indicate here the possible ranges in the hypothesis that *two* large gaps are present, although difficult to discern. Only detailed angle-resolved photoemission spectroscopy (ARPES) measurements can possibly disentangle the energy gaps residing on each sheet of the Fermi surface.

#### IV. $^{75}\text{As}$ NMR RESULTS: ROLE OF SPIN FLUCTUATIONS

While PCARS provides detailed information on the nature and value of the superconducting gaps, NMR can be used to investigate also the normal-state properties of PrFeAs(O,F). Here, we employ mostly  $^{75}\text{As}$ -NMR measurements at 7 T to determine the static (line widths and shifts), as well as the dynamic (spin-lattice relaxation) electronic properties of PrFeAs(O,F). The very small size of the single crystals implied a rather poor S/N ratio. Therefore, the NMR measurements had to be performed on powder samples (obtained by crushing the available single crystals).

Since  $^{75}\text{As}$  has a nuclear spin  $I = 3/2$  with a moderately large quadrupole moment ( $Q = 31.4 \text{ fm}^2$ ), the observed NMR line consists of the central Zeeman  $+1/2$  to  $-1/2$  transition broadened by a second-order quadrupole perturbation, while the two satellites are much too weak and far apart. Both the two-peak lineshape (see Fig. 7) and its variation with temperature (at least down to 40 K) are similar to those of the  $^{75}\text{As}$  NMR lines observed in lightly F-doped LaFeAsO [34,35] or in pure ThFeAsO [36].

##### A. NMR lineshapes and lack of magnetic order

As shown in Fig. 7, down to  $T_c$  ( $\sim 15$  K at 7 T), the position of the NMR lines does not change significantly with temperature, hence suggesting the absence of a magnetic order. This is in agreement with the magnetometry results which, above  $T_c$ , also show a weak and almost flat response. Below  $T_c$ , instead, the NMR lines do not exhibit the expected drop

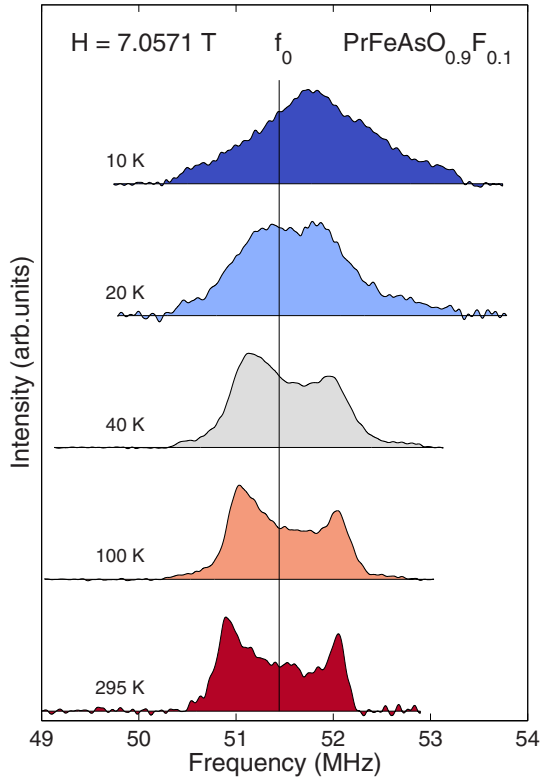


FIG. 7. Frequency-swept  $^{75}\text{As}$  NMR spectra in PrFeAs(O,F), measured at 7 T. The lines refer to the  $^{75}\text{As}$  central transition whose features reflect a second-order quadrupole broadening. While down to  $T_c$  the line width is relatively insensitive to temperature, its position shifts towards higher frequencies (especially below  $T_c$ ). The vertical line indicates the reference  $^{75}\text{As}$ -NMR frequency.

in frequency in the superconducting phase. Indeed, we find that the lines maintain their position, or even show a slight increase in frequency (see, e.g., the dataset at 10 K). This puzzling behavior has been observed also in other iron-based superconductors [37,38], with a possible explanation invoking the multiband structure of such materials. In fact, the Knight-shift part due to the electronic spins can be decomposed into two components:  $K_{\text{spin}} = A_s \chi_s + A_{\text{cp}} \chi_{\text{non-s}}$ , with  $A_s$  the direct Fermi-contact hyperfine coupling to the  $s$ -electrons and  $A_{\text{cp}}$  arising from the core polarization of the inner  $s$ -shells due to non- $s$  (e.g.,  $p$  or  $d$ ) electrons [39]. If  $\chi_{\text{non-s}}$  is strongly temperature dependent,  $K_{\text{spin}}$  changes accordingly and, possibly, even reverses its sign. The multiband structure of 1111 compounds makes things even more complicated since, in this case, the spin susceptibility from each band may exhibit a different temperature response, depending on the overlap of the core with  $p$ -orbitals of the As ion. In addition, in our case, the increasing influence of the magnetic  $\text{Pr}^{3+}$  ions at low temperature might also explain the observed increase in frequency below around 20 K. Indeed, significant  $^{75}\text{As}$  shifts of about +1.5% have been observed also in single-crystal NMR studies of  $\text{CeFeAsO}_{0.8}\text{F}_{0.2}$ , in particular for  $H \parallel c$  [40].

As for the NMR linewidths, these too are similar to those of analogous compounds (see references above), mostly in terms of the full width at half maximum (FWHM) value (here

typically around 1.30 MHz), but less in terms of its temperature dependence. Also in the PrFeAs(O,F) case we observe a moderate increase of FWHM with decreasing temperature (indicative of enhanced magnetic spin fluctuations). However, unlike the generic case, here the two-peaked  $^{75}\text{As}$  central transition shows a progressive broadening of the peaks, which at the same time become closer, until they merge below around 15 K. While these contrasting trends leave the global FWHM practically unchanged, the clear change in line shape indicates a progressive enhancement of the  $\text{Pr}^{3+}$  magnetic effects at low temperature, reflected also in the  $1/T_1$  relaxation rates (see below). Since the observed increase of FWHM is smooth, this is in sharp contrast with the abrupt changes expected in the case of a magnetic phase transition [41]. The lack of appreciable variations of FWHM versus  $T$  strongly suggests that PrFeAs(O,F) does not exhibit any AF order but, at the same time, it may sustain AF fluctuations, as we show in detail below. Finally, note that, in our case, the linewidth broadening may also arise from quadrupole effects, mostly reflecting disorder or defects intrinsic to doped samples. However, comparisons of pure-NQR with NMR spectra have shown that the former is of secondary importance and does not lead to the observed temperature dependence [42]. In particular, the quadrupole broadening is quantitatively less pronounced for the central  $+1/2$  to  $-1/2$  transition, affected only to second order by the quadrupole effects.

## B. NMR relaxation rates and spin fluctuations

$^{57}\text{Fe}$  Mössbauer spectroscopy studies on the PrFeAsO parent compound found an itinerant  $3d$  magnetic order of  $\text{Fe}^{2+}$  ions, with an onset at about 165 K, accompanied by an orthorhombic distortion of the unit cell [43]. Upon lowering the temperature, this evolves into a complete longitudinal incommensurate spin-density-wave (SDW) order below 139 K. At much lower temperatures (12.8 K) also the localized  $\text{Pr}^{3+}$  magnetic ions order. Although the critical temperature of this second magnetic system depends on the type of rare-earth [12], such phenomenology is common to many 1111 parent compounds. Upon F doping, the SDW magnetism is expected to vanish, yet the spin fluctuations to survive. Indeed, as we show below, in the lightly doped PrFeAs(O,F) case, the  $^{75}\text{As}$  NMR spin-lattice relaxation shows clear signatures of strong magnetic fluctuations [44].

The  $^{75}\text{As}$  spin-lattice relaxation times  $T_1$  were evaluated from the magnetization recovery curves recorded on the left-most peak (at around 50.97 MHz) at different temperatures. One of such curves, for  $T = 100$  K, is shown in the inset of Fig. 8(a). The  $T_1$  value for the central transition of a spin-3/2  $^{75}\text{As}$  nucleus is obtained via [45]

$$M_z(t) = M_z^0 [1 - f(0.9e^{(-6t/T_1)^\beta} + 0.1e^{(-t/T_1)^\beta})].$$

Here  $M_z^0$  is the magnetization value at thermal equilibrium,  $f$  reflects the efficiency of population inversion (ideally 2), and  $\beta$  is a stretching exponent. Note that, while the reported data exhibit an almost ideal  $\beta \sim 1$  value, at lower temperatures, due to intrinsic disorder induced by F-doping,  $\beta$  decreases significantly [see Fig. 8(a)]. Under these circumstances, a low  $\beta$  value indicates a wide distribution of relaxation rates. Indeed, as the temperature is lowered, the inequivalence among



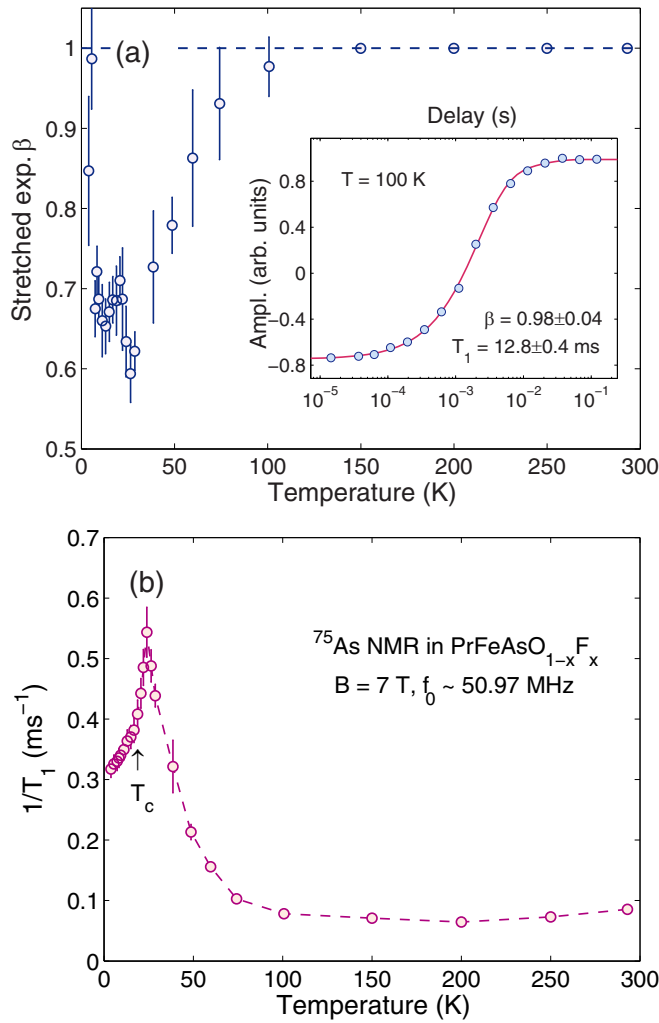


FIG. 8. (a) Stretched-exponential coefficient  $\beta$  vs temperature. Below 100 K,  $\beta$  deviates increasingly from 1 (dashed line). Inset: recovery of magnetization during a typical  $^{75}\text{As}$  NMR  $T_1$  measurement at 100 K. (b) Temperature dependence of the  $^{75}\text{As}$  NMR relaxation rate  $1/T_1$ , measured at 7 T. Below 100 K, the relaxation (dominated by spin fluctuations) becomes increasingly faster and peaks at 24 K, i.e., well above  $T_c$  (see arrow). In the superconducting phase, the behavior is not exponential and  $1/T_1$  saturates at a nonzero value, here reflecting the presence of  $\text{Pr}^{3+}$  magnetic ions.

the NMR sites increases. This implies a broader range of relaxation rates, in turn reflected in a decrease of  $\beta$  from 1 (the ideal value in disorder-free metals) to about 0.65 at low temperature. The final upturn of  $\beta$  close to 0 K is not yet clear. Similar results have been found in the La-1111 family [38] where, by systematically investigating samples across a large doping range, one can clearly correlate  $\beta$  with the degree of disorder.

Our most important results are shown in Fig. 8(b), where we report the evolution of the spin-lattice relaxation rate with temperature. We recall that  $1/T_1$  probes directly the fluctuations of the hyperfine fields at a nuclear site since it is proportional to the  $q$ -summed value of  $\chi''$ , where  $\chi''(q, \omega)$  is the imaginary part of the dynamical electronic susceptibility [39]. The conspicuous increase of  $1/T_1$  upon lowering

temperature is clear evidence of the increasing importance of electronic spin fluctuations at low  $T$ . Such fluctuations are nothing but a residual of the original SDW magnetic order present in the undoped parent compound [44]. Indeed, it has been postulated that optimally doped samples strike a balance between the competing AF phase at lower dopings and the too-weak fluctuations to sustain superconductivity at higher dopings. Our results confirm such a scenario also for the Pr-1111 case.

Let us now discuss the NMR relaxation data in more detail. As the temperature is lowered from room temperature, first we observe a gradual increase of fluctuations, peaking at a cusp-like maximum above  $T_c$ , followed by an abrupt decrease at low temperatures. If we compare our results to those obtained in similar  $\text{Ln}1111$  compounds with different dopings [38,44], it emerges that parent — or very low doped — compounds show a diverging behavior at  $T_{\text{SDW}}$ , while overdoped samples show a very weak peak at  $T_c$ . Our case, closer to optimal doping (given the relatively high  $T_c$ ), indicates that in  $\text{PrFeAs}(\text{O},\text{F})$  spin fluctuations are still dominant down to  $T_c$ . They would continue growing as the suppressed SDW is shifted towards 0 K, but a change in the physics of the system close to  $T_c$  clearly changes also their behavior. While in the undoped case, such an event would be the opening of a SDW gap, in our case, the possibilities seem restricted to the intervening SC phase. However, since the  $1/T_1$  peak occurs at 25 K, i.e., 10 K above  $T_c$  ( $\sim 15$  K at 7 T), the most likely explanation for its occurrence might be given by the Bloembergen-Purcell-Pound model [46], as observed also in other under or optimally doped La-1111 compounds [47]. Such model describes the behavior of the spin-lattice relaxation rate  $1/T_1$  under the influence of local fluctuating magnetic fields  $h(t)$  and indeed predicts a peak in  $1/T_1$  at the temperature where the effective correlation time of the spin fluctuations  $\tau_c$  equals the inverse of the Larmor frequency  $\omega_L$ . Considering the similarity of  $\text{PrFeAs}(\text{O},\text{F})$  with other  $\text{Ln}1111$  compounds, we expect the BPP model to apply also in our case. Here, the particularly sharp cusp in  $1/T_1$  might reflect the joint effect of the  $\text{Fe}^{2+}$  and  $\text{Pr}^{3+}$  spin fluctuations.

Finally, we consider the  $1/T_1$  behavior below  $T_c$ . Given the high quality of data, normally one could use them to study the superconducting gap and pairing. Unfortunately, close to 0 K, the  $1/T_1$  data converge at 0.3  $\text{s}^{-1}$  and not at zero, as expected for a superconductor. In fact, deep in the SC phase, all electrons are bound into Cooper pairs, making the hyperfine interactions with the nuclei a very inefficient relaxation mechanism and driving the relaxation rate to zero. In our case, the finite value of  $1/T_1(0)$  indicates that, at very low temperatures, other relaxation mechanisms are at play. This excludes a possible use of the data collected in the SC phase and explains why here we limited our NMR study to the normal phase. Among the alternative relaxation mechanisms one could think of disorder-related relaxation channels (intrinsic to doping). However, a comparison to La-1111 results [38,47] excludes it since compounds with widely different dopings still exhibit a  $1/T^3$  behavior at low  $T$ . On the other hand, the presence of a magnetic ion, such as  $\text{Pr}^{3+}$ , could well justify our results. Indeed, an almost identical dependence of the  $^{75}\text{As}$  NMR relaxation rate versus temperature is also found in the Ce-1111 case [40]. We recall that Ce, Pr, and Nd have

similar magnetic moments (free-ion values of 2.54, 3.58, and 3.62  $\mu_B$ , respectively), whose strong coupling with Fe spin fluctuations in the FeAs layer could explain our results, as well as the different low- $T$  behavior of relaxation compared to the nonmagnetic La-1111 case.

## V. CONCLUSION

By combining point-contact Andreev spectroscopy with nuclear magnetic resonance methods we investigated in detail the normal and superconducting state properties of underdoped PrFeAs(O,F), a member of the  $Ln1111$  family. Point-contact Andreev spectroscopy performed on single crystals provides evidence of the multiband/multigap nature of the PrFeAs(O,F) superconductivity. No indications of low-energy quasiparticles were found in the point-contact spectra, suggesting a fully gapped superconductor with no nodes. A small  $\Delta_1 \simeq 3.5 \pm 0.5$  meV gap was found not only to be very robust, but also to agree well with the results of microwave penetration depth and quasiparticle conductivity measurements [19]. Additional structures, in the form of conductance maxima or shoulders, could be interpreted as being due to one or possibly two larger gaps, whose amplitudes lie in the energy ranges  $\simeq 6.0$ – $7.5$  meV (in agreement with optical conductivity measurements [20]) and  $\simeq 8$ – $10$  meV. The later values are quite large and would correspond to gap ratios  $2\Delta/k_B T_c$  of the order of 9. Moreover, we showed that additional high-energy structures, ubiquitous in the conductance curves and not predicted by any BCS-based theory, are the hallmark of *strong coupling* between the electrons and spin fluctuations and can only be accounted for in the framework of a strong-coupling theory of superconductivity. Finally, magnetic resonance results in the normal phase provide clear evidence about the lack of any magnetic order in PrFeAs(O,F). Further, spin-lattice relaxation data suggest that this compound, similarly to other members of the 1111 family, hosts substantial electronic spin fluctuations (here enhanced by the presence of  $\text{Pr}^{3+}$  ions), which are expected to mediate the superconducting pairing.

## ACKNOWLEDGMENTS

G.A.U. acknowledges support from the MEPHI Academic Excellence Project (Contract No. 02.a03.21.0005). This work was partly supported by the Swiss National Science Foundation (SNSF) through Grant No. 200021-169455.

## APPENDIX A: BASICS OF THE PCARS TECHNIQUE

To ensure proper PCARS measurement conditions, the contact must be smaller than the electronic mean free path, so that the conduction is ballistic, no Joule dissipation occurs in the contact region, and the resistance of the contact largely exceeds the resistance of the normal bank [26]. In these conditions, the voltage drop at the N/S interface practically coincides with the total potential difference between the electrodes  $V$  and the excess energy with which electrons are injected in the  $S$  side of the junction is just  $eV$ . Provided that there is no insulating layer at the sample surface, the conduction is dominated by the Andreev reflection [27,48], even though the probability of quasiparticle tunneling is not zero.

The raw  $dI/dV$ -versus- $V$  spectrum already contains qualitative information on the number, amplitude, and symmetry of the gap(s). However, a more quantitative analysis can be made by fitting it with suitable models for the Andreev reflection at the N/S interface [27,28].

To fabricate the contacts, we used the so-called “soft” technique, widely described elsewhere [26,49]. In a few words, we stretch a thin Au wire over the crystal, until it touches the surface in a single point. Typically, ballistic contacts have resistances of a few tens of Ohms (even though the actual value depends on the properties of the sample, namely on its normal-state resistivity). These types of contacts can be mechanically unstable, especially during cooling/heating, because of the different thermal coefficients of the materials. Thus, in some cases, we used a drop of conducting Ag glue to improve the stability. Independent of the presence of Ag glue, the actual contact must be thought of as a parallel of nanoscopic contacts between a normal metal and a superconductor.

## APPENDIX B: STRONG-COUPLING MODEL FOR THE SUPERCONDUCTIVITY IN PR-1111

As already mentioned, one can account for the presence of electron-boson structures only by using a strong-coupling extension of the BCS theory, i.e., the Eliashberg theory. Based on the similarity to other electron-doped Fe-based superconductors, we assume Pr-1111 to be described by an effective  $s\pm$ -wave three-band model [50–53], with one hole-like band centered at  $\Gamma$  and two electron-like Fermi surface sheets at the corners of the Brillouin zone. This model is described in detail elsewhere [30,54].

To calculate the SC gaps and the critical temperature in this model, one has to solve six coupled equations for the complex order parameters  $\Delta_i(i\omega_n)$  and the renormalization functions  $Z_i(i\omega_n)$ , where  $i = 1, 2, 3$  is the band index and  $\omega_n$  are the Matsubara frequencies. The frequency (energy) dependence of the order parameters, normally ignored in the BCS theory, is here the key factor that accounts for the presence of the electron-boson coupling features. There are many input parameters, including (i) nine electron-phonon spectral functions,  $\alpha_{ij}^2 F^{ph}(\Omega)$ ; (ii) nine electron-boson (spin fluctuations) spectral functions,  $\alpha_{ij}^2 F^{sf}(\Omega)$ ; (iii) nine elements of the Coulomb pseudopotential matrix,  $\mu_{ij}^*(\omega_c)$ . To a first approximation, we neglect the disorder, thus assuming that all the scattering rates (from either magnetic or nonmagnetic impurities) are zero. To further simplify the problem, some additional assumptions can be made, shown to be valid in the case of iron pnictides [54–56]. In particular, we know that phonons do not contribute significantly to the (dominant) interband coupling [50] (i.e.,  $\lambda_{ij}^{ph} \approx 0$ ) and that the total electron-phonon coupling constant is small [57]. Hence, we can simply neglect the phonon contribution and assume  $\lambda_{ii}^{ph} = 0$ . Spin fluctuations, instead, are known to provide mostly the *interband* coupling between the hole and electron bands, so we can assume  $\lambda_{ii}^{sf} = 0$ . Finally, following Ref. [58], we will assume that the Coulomb pseudopotential matrix is identically zero, i.e.,  $\mu_{ii}^*(\omega_c) = \mu_{ij}^*(\omega_c) = 0$ . With these approximations, the electron-boson coupling-constant matrix  $\lambda_{ij}$

becomes [50,54–56]

$$\lambda_{ij} = \begin{pmatrix} 0 & \lambda_{12}^{sf} & \lambda_{13}^{sf} \\ 0 & \lambda_{21}^{sf} = \lambda_{12}^{sf} \nu_{12} & 0 \\ \lambda_{31}^{sf} = \lambda_{13}^{sf} \nu_{13} & 0 & 0 \end{pmatrix}, \quad (\text{B1})$$

where  $\nu_{ij} = N_i(0)/N_j(0)$ , with  $N_i(0)$  the normal density of states at the Fermi level for the  $i$ th band. The electron-boson coupling constants are defined through the Eliashberg functions  $\alpha_{ij}^2 F_{ij}^{sf}(\Omega)$ . Following Refs. [54–56] we choose these functions to have a Lorentzian shape, with a maximum at the energy  $\Omega_0$  and half-width  $\Omega_0/2$ .  $\Omega_0$  is the characteristic energy of the mediating boson, which corresponds to the characteristic energy of the spin resonance [33] and is related to the critical temperature by the empirical law  $\Omega_0 = 2T_c/5$  that has been demonstrated to hold, at least approximately, for many iron pnictides [59].

The factors  $\nu_{ij}$  that enter the definition of  $\lambda_{ij}$  can normally be determined from the band-structure calculations, unfortunately not available for the Pr-1111 case. However, since our aim is just to show that the wide shoulders observed in our datasets [we will refer in particular to the data in Fig. 4(b)] are due to electron-boson coupling, we may use the values employed in Co-doped Ba-122 [56] (because this also is an electron-doped Fe-based superconductor with a similar  $T_c$ ), i.e.,  $\nu_{12} = 1.12$  and  $\nu_{13} = 4.50$ . Hence, only two free parameters remain,  $\lambda_{12}$  and  $\lambda_{13}$ , that need to be fixed to reproduce the experimental  $T_c$  and the experimental gaps. We find  $\lambda_{12} = 0.7$  and  $\lambda_{13} = 1.8$ , giving a total coupling constant  $\lambda_t = 2.374$ .

Owing to the  $s\pm$  symmetry, the order parameter has opposite signs on the hole-like and the electron-like Fermi surface sheets. The low-temperature values of the gaps turn out to be  $\Delta_h = 6.33$  meV,  $\Delta_{e1} = 3.35$  meV, and  $\Delta_{e2} = 8.56$  meV, where the subscripts  $h$  and  $e$  refer to the hole-like and electron-like Fermi surfaces, respectively. The gap values agree very well with the gap distribution shown in Fig. 6. The calculated critical temperature is  $T_c = 28.6$  K. This value is slightly larger than the onset of the superconducting transition (see Fig. 1). However, since the coupling is of electronic origin, there is a feedback effect of the SC condensate on the spin-fluctuation spectrum [52,53]. Taking this effect into account, as we already did in Ref. [56], the critical temperature turns out to be  $T_c = 22.86$  K. Once the order parameters as a function of energy are known, they can be inserted

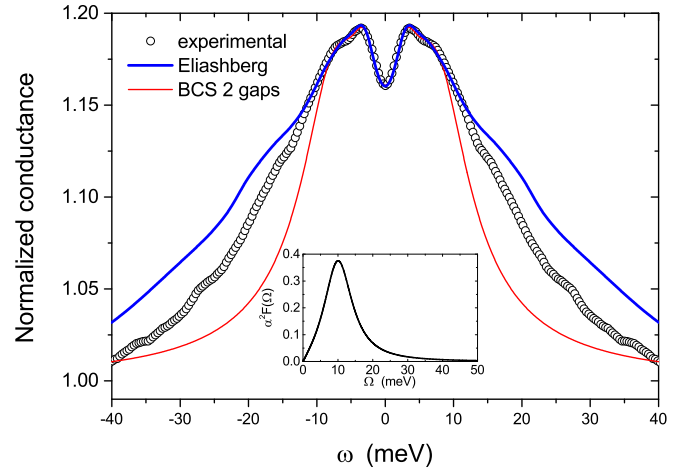


FIG. 9. Open circles: experimental data reported in Fig. 4(b). Blue line: calculated curve after inserting into the three-band BTK-like model the energy-dependent order parameters, calculated by solving the Eliashberg equations. The red line is a fit of the theoretical curve with a two-band BCS-based BTK model (with constant gaps), which reproduces the same gap values as in Fig. 4(b) (red curve). The inset shows the electron-boson spectral function for the antiferromagnetic spin fluctuations, here normalized to have  $\lambda = 1$ .

into the equations for the Andreev reflection (i.e., in the three-band version of the BTK model) and the conductance curve can be calculated. The BTK model contains, in addition to the gap amplitudes, the relative weights of the bands, the barrier parameters, and the broadening parameters. We chose the values of these parameters to obtain a curve similar to that in Fig. 4(b). In particular, we took  $Z_h = Z_{e1} = Z_{e2} = 0.33$ ,  $\Gamma_h = 2.95$  meV,  $\Gamma_{e1} = 1.45$  meV,  $\Gamma_{e2} = 4.05$  meV,  $w_h = 0.20$ ,  $w_{e1} = 0.25$ , and  $w_{e2} = 0.55$ . The resulting curve is shown in Fig. 9 with a blue line. Clearly, accounting for the energy dependence of the order parameters gives rise to very wide (in energy) and very high (in amplitude) shoulders that resemble very closely those of the experimental data (actually, a proper normalization could easily reproduce an experimental spectrum with the same shape), but does not affect the low-energy part of the spectrum, where the gap-related features show up. Indeed, the fit of the theoretical curve with the same two-band BTK model we used to fit the experimental data would have given again  $\Delta_1 = 3.3$  meV and  $\Delta_2 = 8.5$  meV.

- [1] Y. Kamihara, T. Watanabe, M. Hirano, and H. Hosono, Iron-based layered superconductor  $\text{La}[\text{O}_{1-x}\text{F}_x]\text{FeAs}$  ( $x = 0.05\text{--}0.12$ ) with  $T_c = 26$  K, *J. Am. Chem. Soc.* **130**, 3296 (2008).
- [2] S. Iimura, S. Matsuishi, H. Sato, T. Hanna, Y. Muraba, S. W. Kim, J. E. Kim, M. Takata, and H. Hosono, Two-dome structure in electron-doped iron arsenide superconductors, *Nat. Commun.* **3**, 943 (2012).
- [3] T. E. Kuzmicheva, S. A. Kuzmichev, and N. D. Zhigadlo, Superconducting order parameter and bosonic mode in hydrogen-substituted  $\text{NdFeAsO}_{0.6}\text{H}_{0.36}$  revealed by multiple Andreev-reflection spectroscopy, *Phys. Rev. B* **100**, 144504 (2019).

- [4] R. Khasanov, S. Sanna, G. Prando, Z. Shermadini, M. Bendele, A. Amato, P. Carretta, R. De Renzi, J. Karpinski, S. Katrych, H. Luetkens, and N. D. Zhigadlo, Tuning of competing magnetic and superconducting phase volumes in  $\text{LaFeAsO}_{0.945}\text{F}_{0.055}$  by hydrostatic pressure, *Phys. Rev. B* **84**, 100501(R) (2011).
- [5] H.-H. Wen, G. Mu, L. Fang, H. Yang, and X. Zhu, Superconductivity at 25 K in hole-doped  $(\text{La}_{1-x}\text{Sr}_x)\text{OFeAs}$ , *Europhys. Lett.* **82**, 17009 (2008).
- [6] G. Mu, B. Zeng, X. Zhu, F. Han, P. Cheng, B. Shen, and H.-H. Wen, Synthesis, structural, and transport properties of the

- hole-doped superconductor  $\text{Pr}_{1-x}\text{Sr}_x\text{FeAsO}$ , *Phys. Rev. B* **79**, 104501 (2009).
- [7] C. Wang, L. Li, S. Chi, Z. Zhu, Z. Ren, Y. Li, Y. Wang, X. Lin, Y. Luo, S. Jiang, X. Xu, G. Cao, and Z. Xu, Thorium-doping-induced superconductivity up to 56 K in  $\text{Gd}_{1-x}\text{Th}_x\text{FeAsO}$ , *Europhys. Lett.* **83**, 67006 (2008).
- [8] N. D. Zhigadlo, S. Katrych, S. Weyeneth, R. Puzniak, P. J. W. Moll, Z. Bukowski, J. Karpinski, H. Keller, and B. Batlogg, Th-substituted  $\text{SmFeAsO}$ : Structural details and superconductivity with  $T_c$  above 50 K, *Phys. Rev. B* **82**, 064517 (2010).
- [9] C. Wang, S. Jiang, Q. Tao, Z. Ren, Y. Li, L. Li, C. Feng, J. Dai, G. Cao, and Z. Xu, Superconductivity in  $\text{LaFeAs}_{1-x}\text{P}_x\text{O}$ : Effect of chemical pressures and bond covalency, *Europhys. Lett.* **86**, 47002 (2009).
- [10] N. D. Zhigadlo, S. Katrych, M. Bendele, P. J. W. Moll, M. Tortello, S. Weyeneth, V. Y. Pomjakushin, J. Kanter, R. Puzniak, Z. Bukowski, H. Keller, R. S. Gonnelli, R. Khasanov, J. Karpinski, and B. Batlogg, Interplay of composition, structure, magnetism, and superconductivity in  $\text{SmFeAs}_{1-x}\text{P}_x\text{O}_{1-y}$ , *Phys. Rev. B* **84**, 134526 (2011).
- [11] A. J. Drew, C. Niedermayer, P. J. Baker, F. L. Platt, S. J. Blundell, T. Lancaster, R. H. Liu, G. Wu, X. H. Chen, I. Watanabe, V. K. Malik, A. Dubroka, M. Rössle, K. W. Kim, C. Baines, and C. Bernhard, Coexistence of static magnetism and superconductivity in  $\text{SmFeAsO}_{1-x}\text{F}_x$  as revealed by muon spin rotation, *Nat. Mater.* **8**, 310 (2009).
- [12] S. Sanna, R. De Renzi, G. Lamura, C. Ferdeghini, A. Palenzona, M. Putti, M. Tropeano, and T. Shiroka, Magnetic-superconducting phase boundary of  $\text{SmFeAsO}_{1-x}\text{F}_x$  studied via muon spin rotation: Unified behavior in a pnictide family, *Phys. Rev. B* **80**, 052503 (2009).
- [13] G. Lamura, T. Shiroka, P. Bonfà, S. Sanna, R. De Renzi, M. Putti, N. D. Zhigadlo, S. Katrych, R. Khasanov, and J. Karpinski, Slow magnetic fluctuations and superconductivity in fluorine-doped  $\text{NdFeAsO}$ , *Phys. Rev. B* **91**, 024513 (2015).
- [14] C. R. Rotundu, D. T. Keane, B. Freelon, S. D. Wilson, A. Kim, P. N. Valdivia, E. Bourret-Courchesne, and R. J. Birgeneau, Phase diagram of the  $\text{PrFeAsO}_{1-x}\text{F}_x$  superconductor, *Phys. Rev. B* **80**, 144517 (2009).
- [15] H. Luetkens, H.-H. Klauss, M. Kraken, F. J. Litterst, T. Dellmann, R. Klingeler, C. Hess, R. Khasanov, A. Amato, C. Baines, M. Kosmala, O. J. Schumann, M. Braden, J. Hamann-Borrero, N. Leps, A. Kondrat, G. Behr, J. Werner, and B. Büchner, The electronic phase diagram of the  $\text{LaO}_{1-x}\text{F}_x\text{FeAs}$  superconductor, *Nat. Mater.* **8**, 305 (2009).
- [16] N. D. Zhigadlo, S. Weyeneth, S. Katrych, P. J. W. Moll, K. Rogacki, S. Bosma, R. Puzniak, J. Karpinski, and B. Batlogg, High-pressure flux growth, structural, and superconducting properties of  $\text{LnFeAsO}$  ( $\text{Ln} = \text{Pr, Nd, Sm}$ ) single crystals, *Phys. Rev. B* **86**, 214509 (2012).
- [17] N. D. Zhigadlo, Growth of whisker-like and bulk single crystals of  $\text{PrFeAs(O,F)}$  under high pressure, *J. Cryst. Growth* **382**, 75 (2013).
- [18] J. Karpinski, N. Zhigadlo, S. Katrych, Z. Bukowski, P. Moll, S. Weyeneth, H. Keller, R. Puzniak, M. Tortello, D. Daghero, R. Gonnelli, I. Maggio-Aprile, Y. Fasano, Ø. Fischer, K. Rogacki, and B. Batlogg, Single crystals of  $\text{LnFeAsO}_{1-x}\text{F}_x$  ( $\text{Ln} = \text{La, Pr, Nd, Sm, Gd}$ ) and  $\text{Ba}_{1-x}\text{Rb}_x\text{Fe}_2\text{As}_2$ : Growth, structure and superconducting properties, *Physica C* **469**, 370 (2009).
- [19] K. Hashimoto, T. Shibauchi, T. Kato, K. Ikada, R. Okazaki, H. Shishido, M. Ishikado, H. Kito, A. Iyo, H. Eisaki, S. Shamoto, and Y. Matsuda, Microwave Penetration Depth and Quasiparticle Conductivity of  $\text{PrFeAsO}_{1-y}$  Single Crystals: Evidence for a Full-Gap Superconductor, *Phys. Rev. Lett.* **102**, 017002 (2009).
- [20] A. Charnukha, D. Pröpper, N. D. Zhigadlo, M. Naito, M. Schmidt, Z. Wang, J. Deisenhofer, A. Loidl, B. Keimer, A. V. Boris, and D. N. Basov, Intrinsic Charge Dynamics in High- $T_c$   $\text{AFeAs(O,F)}$  Superconductors, *Phys. Rev. Lett.* **120**, 087001 (2018).
- [21] R. S. Gonnelli, D. Daghero, M. Tortello, G. A. Ummarino, V. A. Stepanov, J. S. Kim, and R. K. Kremer, Coexistence of two order parameters and a pseudogap-like feature in the iron-based superconductor  $\text{LaFeAsO}_{1-x}\text{F}_x$ , *Phys. Rev. B* **79**, 184526 (2009).
- [22] D. Daghero, M. Tortello, R. S. Gonnelli, V. A. Stepanov, N. D. Zhigadlo, and J. Karpinski, Evidence for two-gap nodeless superconductivity in  $\text{SmFeAsO}_{1-x}\text{F}_x$  from point-contact Andreev-reflection spectroscopy, *Phys. Rev. B* **80**, 060502(R) (2009).
- [23] R. S. Gonnelli, D. Daghero, M. Tortello, G. Ummarino, Z. Bukowski, J. Karpinski, P. G. Reuvekamp, R. K. Kremer, G. Profeta, K. Suzuki, and K. Kuroki, Fermi-surface topological phase transition and horizontal order-parameter nodes in  $\text{CaFe}_2\text{As}_2$  under pressure, *Sci. Rep.* **6**, 26394 (2016).
- [24] R. S. Gonnelli, M. Tortello, D. Daghero, R. K. Kremer, Z. Bukowski, N. D. Zhigadlo, and J. Karpinski, Point-contact spectroscopy in Co-doped  $\text{CaFe}_2\text{As}_2$ : Nodal superconductivity and topological Fermi surface transition, *Supercond. Sci. Tech.* **25**, 065007 (2012).
- [25] K. Matano, Z. A. Ren, X. L. Dong, L. L. Sun, Z. X. Zhao, and G.-q. Zheng, Spin-singlet superconductivity with multiple gaps in  $\text{PrFeAsO}_{0.89}\text{F}_{0.11}$ , *Europhys. Lett.* **83**, 57001 (2008).
- [26] D. Daghero and R. S. Gonnelli, Probing multiband superconductivity by point-contact spectroscopy, *Supercond. Sci. Tech.* **23**, 043001 (2010).
- [27] G. E. Blonder, M. Tinkham, and T. M. Klapwijk, Transition from metallic to tunneling regimes in superconducting microconstrictions: Excess current, charge imbalance, and supercurrent conversion, *Phys. Rev. B* **25**, 4515 (1982).
- [28] S. Kashiwaya, Y. Tanaka, M. Koyanagi, and K. Kajimura, Theory for tunneling spectroscopy of anisotropic superconductors, *Phys. Rev. B* **53**, 2667 (1996).
- [29] M. Tortello, D. Daghero, G. A. Ummarino, V. A. Stepanov, J. Jiang, J. D. Weiss, E. E. Hellstrom, and R. S. Gonnelli, Multigap Superconductivity and Strong Electron-Boson Coupling in Fe-Based Superconductors: A Point-Contact Andreev-Reflection Study of  $\text{Ba(Fe}_{1-x}\text{Co}_x)_2\text{As}_2$  Single Crystals, *Phys. Rev. Lett.* **105**, 237002 (2010).
- [30] D. Daghero, M. Tortello, G. A. Ummarino, and R. S. Gonnelli, Directional point-contact Andreev-reflection spectroscopy of Fe-based superconductors: Fermi surface topology, gap symmetry, and electron-boson interaction, *Rep. Prog. Phys.* **74**, 124509 (2011).
- [31] D. Daghero, P. Pecchio, G. A. Ummarino, F. Nabeshima, Y. Imai, A. Maeda, I. Tsukada, S. Komiya, and R. S. Gonnelli, Point-contact Andreev-reflection spectroscopy in  $\text{Fe(Te,Se)}$  films: Multiband superconductivity and electron-boson coupling, *Supercond. Sci. Tech.* **27**, 124014 (2014).



- [32] W. L. McMillan and J. M. Rowell, Tunnelling and strong-coupling superconductivity, in *Superconductivity*, edited by R. D. Parks, (Marcel Dekker, New York, 1969), Vol. 1, Chap. 11, pp. 561–614.
- [33] D. S. Inosov, J. T. Park, P. Bourges, D. L. Sun, Y. Sidis, A. Schneidewind, K. Hradil, D. Haug, C. T. Lin, B. Keimer, and V. Hinkov, Normal-state spin dynamics and temperature-dependent spin-resonance energy in optimally doped  $\text{BaFe}_{1.85}\text{Co}_{0.15}\text{As}_2$ , *Nat. Phys.* **6**, 178 (2010).
- [34] H.-J. Grafe, D. Paar, G. Lang, N. J. Curro, G. Behr, J. Werner, J. Hamann-Borrero, C. Hess, N. Leps, R. Klingeler, and B. Büchner,  $^{75}\text{As}$  NMR Studies of Superconducting  $\text{LaFeAsO}_{0.9}\text{F}_{0.1}$ , *Phys. Rev. Lett.* **101**, 047003 (2008).
- [35] Y. Nakai, S. Kitagawa, K. Ishida, Y. Kamihara, M. Hirano, and H. Hosono, An NMR study on the F-doping evolution of the iron oxypnictide  $\text{LaFeAs}(\text{O}_{1-x}\text{F}_x)$ , *New J. Phys.* **11**, 045004 (2009).
- [36] T. Shiroka, T. Shang, C. Wang, G.-H. Cao, I. Eremin, H.-R. Ott, and J. Mesot, High- $T_c$  superconductivity in undoped  $\text{ThFeAsN}$ , *Nat. Commun.* **8**, 156 (2017).
- [37] H. Mukuda, F. Engetsu, T. Shiota, K. T. Lai, M. Yashima, Y. Kitaoka, S. Miyasaka, and S. Tajima, Emergence of novel anti-ferromagnetic order intervening between two superconducting phases in  $\text{LaFe}(\text{As}_{1-x}\text{P}_x)\text{O}$ :  $^{31}\text{P}$  -NMR studies, *J. Phys. Soc. Jpn.* **83**, 083702 (2014).
- [38] T. Shiroka, N. Barbero, R. Khasanov, N. D. Zhigadlo, H.-R. Ott, and J. Mesot, Nodal-to-nodeless superconducting order parameter in  $\text{LaFeAs}_{1-x}\text{P}_x\text{O}$  synthesized under high pressure, *npj Quant. Mater.* **3**, 25 (2018).
- [39] A. Abragam, *The Principles of Nuclear Magnetism* (Clarendon, Oxford, 1978).
- [40] D. Rybicki, T. Meissner, G. V. M. Williams, S. V. Chong, M. Lux, and J. Haase,  $^{75}\text{As}$  NMR study of overdoped  $\text{CeFeAsO}_{0.8}\text{F}_{0.2}$ , *J. Phys.: Cond. Matter* **25**, 315701 (2013).
- [41] F. Borsa, Phase transitions and critical phenomena in solids, in *eMagRes*, edited by R. K. Harris and R. E. Wasylshen, (John Wiley & Sons, Hoboken, NJ, 2007).
- [42] S. H. Baek, H. J. Grafe, F. Hammerath, M. Fuchs, C. Rudisch, L. Harnagea, S. Aswartham, S. Wurmehl, J. van den Brink, and B. Büchner,  $^{75}\text{As}$  NMR-NQR study in superconducting  $\text{LiFeAs}$ , *Eur. Phys. J. B* **85**, 159 (2012).
- [43] K. Komędera, A. Pierzga, A. Błachowski, K. Ruebenbauer, A. Budziak, S. Katrych, and J. Karpinski, Magnetism of  $\text{PrFeAsO}$  parent compound for iron-based superconductors: Mössbauer spectroscopy study, *J. Alloys Compd.* **717**, 350 (2017).
- [44] K. Ishida, Y. Nakai, S. Kitagawa, and T. Iye, NMR studies on iron-pnictide superconductors:  $\text{LaFeAs}(\text{O}_{1-x}\text{F}_x)$  and  $\text{BaFe}_2(\text{As}_{1-x}\text{P}_x)_2$ , *C. R. Physique* **12**, 515 (2011).
- [45] A. F. McDowell, Magnetization-recovery curves for quadrupolar spins, *J. Magn. Reson. Ser. A* **113**, 242 (1995).
- [46] N. Bloembergen, E. M. Purcell, and R. V. Pound, Nuclear magnetic relaxation, *Nature* **160**, 475 (1948); Relaxation effects in nuclear magnetic resonance absorption, *Phys. Rev.* **73**, 679 (1948).
- [47] F. Hammerath, U. Gräfe, T. Kühne, H. Kühne, P. L. Kuhns, A. P. Reyes, G. Lang, S. Wurmehl, B. Büchner, P. Carretta, and H.-J. Grafe, Progressive slowing down of spin fluctuations in underdoped  $\text{LaFeAsO}_{1-x}\text{F}_x$ , *Phys. Rev. B* **88**, 104503 (2013).
- [48] A. F. Andreev, The thermal conductivity of the intermediate state in superconductors, *J. Exptl. Theor. Phys. (U.S.S.R.)* **46**, 1823 (1964) [*Sov. Phys. JETP* **19**, 1228 (1964)].
- [49] N. D. Zhigadlo, D. Logvinovich, V. A. Stepanov, R. S. Gonnelli, and D. Daghero, Crystal growth, characterization, and point-contact Andreev-reflection spectroscopy of the non-centrosymmetric superconductor  $\text{Mo}_3\text{Al}_2\text{C}$ , *Phys. Rev. B* **97**, 214518 (2018).
- [50] I. I. Mazin and J. Schmalian, Pairing symmetry and pairing state in ferropnictides: Theoretical overview, *Physica C* **469**, 614 (2009).
- [51] G. M. Eliashberg, Interactions between electrons and lattice vibrations in a superconductor, *J. Exptl. Theor. Phys. (U.S.S.R.)* **38**, 666 (1960) [*Sov. Phys. JETP* **11**, 696 (1960)].
- [52] A. V. Chubukov, D. Pines, and J. Schmalian, A spin fluctuation model for  $d$ -wave superconductivity, in *Superconductivity - Conventional and Unconventional Superconductors*, edited by K. Bennemann and J. Ketterson, (Springer, Berlin, 2008), pp. 1349–1413.
- [53] D. Manske, I. Eremin, and K. H. Bennemann, Electronic theory for superconductivity in high- $T_c$  cuprates and  $\text{Sr}_2\text{RuO}_4$ , in *Superconductivity - Conventional and Unconventional Superconductors*, edited by K. Bennemann and J. Ketterson, (Springer, Berlin, 2008), pp. 1415–1515.
- [54] G. A. Ummarino, M. Tortello, D. Daghero, and R. S. Gonnelli, Three-band  $s\pm$  Eliashberg theory and the superconducting gaps of iron pnictides, *Phys. Rev. B* **80**, 172503 (2009).
- [55] G. A. Ummarino, M. Tortello, D. Daghero, and R. S. Gonnelli, Predictions of multiband  $s\pm$  strong-coupling Eliashberg theory compared to experimental data in iron pnictides, *J. Supercond. Nov. Magn.* **24**, 247 (2011).
- [56] G. A. Ummarino, Multiband  $s\pm$  Eliashberg theory and temperature-dependent spin-resonance energy in iron pnictide superconductors, *Phys. Rev. B* **83**, 092508 (2011).
- [57] L. Boeri, M. Calandra, I. I. Mazin, O. V. Dolgov, and F. Mauri, Effects of magnetism and doping on the electron-phonon coupling in  $\text{BaFe}_2\text{As}_2$ , *Phys. Rev. B* **82**, 020506(R) (2010).
- [58] P. J. Hirschfeld, M. M. Korshunov, and I. I. Mazin, Gap symmetry and structure of Fe-based superconductors, *Rep. Prog. Phys.* **74**, 124508 (2011).
- [59] J. Paglione and R. L. Greene, High-temperature superconductivity in iron-based materials, *Nat. Phys.* **6**, 645 (2010).